

Joint radar/lidar observations of possible aerosol layers in the winter mesosphere

K. Stebel^{1*}, U. Blum², K.-H. Fricke², S. Kirkwood¹, N. J. Mitchell³, A. Osepian⁴.

¹ Swedish Institute of Space Physics, Box 812, 981 28 Kiruna, Sweden

² Physics Institute, University of Bonn, Nussallee 12, D-53115 Bonn, Germany

³ Telecommunications, Space and Radio Group, Department of Electronic & Electrical Engineering, University of Bath, Bath BA2 7AY, UK

⁴ Polar Geophysical Institute, Halturina 15, Murmansk, Russia

* now at Norwegian Institute for Air Research, The Polar Environmental Centre, NO-9296 Tromsø, Norway

corresponding author : S. Kirkwood, sheila.kirkwood@irf.se , tel +46 980 79083, fax +46 980 79050

version 7 March 2003

submitted to JASTP 7 march 2003

revised 10 february 2004

Abstract

Narrow layers of enhanced radar echoes from the winter mesosphere have been observed by the ESRAD 52 MHz radar (68° N, 21° E) during recent solar proton events. These layers have been named PMWE, Polar Mesosphere Winter Echoes. Comparison of the characteristics of the radar echoes to the expected characteristics of neutral turbulence in the winter mesosphere leads to the conclusion that PMWE are unlikely to be caused by neutral turbulence alone. Their strength, and their persistence in conditions when moderately high concentrations of negative ions can be expected, are however consistent with the expected influence of small charged aerosol particles on radar scatter. During a solar proton event in January 2002 measurements were made by both the ESRAD radar and a lidar situated at the same site. The lidar observed a region of enhanced backscatter in the same height interval as the radar observed PMWE. The lidar observations can be interpreted either as a sharp temperature minimum or as a layer of aerosol particles. The latter interpretation offers consistency with the radar observations.

Keywords: mesosphere, winter, aerosol particles, radar, lidar, PMWE

Introduction

In a recent paper Kirkwood et al. (2002a) have presented observations of thin layers of enhanced radar echoes in the winter mesosphere made with the ESRAD 52 MHz radar (67.88° N, 21.10° E). The layers were named Polar Mesosphere Winter Echoes (PMWE) since they were observed between 50 km and 80 km altitude during several solar proton events during the winter 2000/2001, but were notably absent during summer-time solar proton events. Figure 1 shows a further example of PMWE recorded with the ESRAD radar during a solar proton event in January 2002.

VHF radar echoes from the high-latitude mesosphere were first reported two decades ago, when they were frequently observed by the much more powerful radars which were then in operation. The first studies using the Poker Flat radar in Alaska (location 65.12° N, 147.43° W, with power-aperture product of $\sim 10^{11}$ Wm², a thousand times higher than ESRAD) were reported by Ecklund and Balsley, 1981 and Balsley et al., 1983. Wintertime echoes were seen between 50 and 80 km and appeared to be

correlated with high-energy particle precipitation enhancing the ionisation in the mesosphere. The echoes were interpreted as due to turbulence caused by breaking gravity waves. However, the limited height resolution of the Poker Flat radar (2.2 km) precluded study of the structure on smaller scales than a few km, and no systematic study was made of the echo dependence on ionisation levels in the surrounding atmosphere. Wintertime echoes at high latitudes were further studied by Czechowsky et al. (1989), using the SOUSY mobile radar during a campaign from Andøya, northern Norway in 1983/84 (location 69.17° N, 16.01° E). Results similar to those from Poker Flat were found and it was confirmed that the echoes were detectable only during periods when electron densities were enhanced by energetic particle precipitation. It was noted that enhanced electron densities during the hours of darkness seemed not to lead to observable echoing layers below about 70 km altitude. Also in this case, the echoing structures were said to have vertical extent of 2-10 km and turbulence due to wave saturation and/or breaking was again proposed as the cause.

Mesospheric echoes observed by the ESRAD, Poker Flat and SOUSY radars, which all operate at frequencies close to 50 MHz, must be caused by fluctuations in electron density with scale sizes of about 3 m. Since the early reports, much more information has become available regarding the nature of turbulence in the high-latitude winter mesosphere from a large number of sounding-rocket measurements (Lübken, 1993; Lübken et al., 1993 ; Lübken 1997). It is now known that there are indeed thin layers of neutral turbulence in the region. However, the fluctuation amplitudes are sharply attenuated for scale sizes less than an 'inner-scale' which has been observed to lie in the range 10-100 m in the winter mesosphere. For the altitude of 70 km, for example, where many PMWE are observed, the inner-scale of neutral turbulence was found in the rocket flights to lie between 20 and 50 m. The inner-scale length depends on the turbulent energy dissipation rate, so, correspondingly the energy dissipation rates were found by Lübken et al.'s work to be rather small, typically 1-10 mW/kg.

In the normal sunlit ionosphere, electron diffusion is controlled by positive ion diffusion and ion diffusivity is close to that of the neutral gas. In this situation, electron density fluctuations are expected to follow the same scale-size spectrum as neutral density fluctuations (Thrane and Grandal, 1981). In other words, electron

density fluctuations at the 3 m scale size needed to cause radar echoes will be substantially attenuated since they are about a factor of 10 smaller than the inner-scale size. Further, as the solar elevation decreases below zero, electrons attach easily to form negative ions, the negative ions now maintain the charge balance with the positive ions and the electrons become free to diffuse much more rapidly (Hill, 1978a). In these conditions, attenuation of electron density fluctuations is expected to start at even longer scale-sizes than for the neutral turbulence (see. e.g. Driscoll and Kennedy, 1985).

Kirkwood et al. (2002a) noted that PMWE were detectable in all electron density conditions (within the modelled range $10^7 - 3 \times 10^{10} \text{ m}^{-3}$) when the ratio of negative ions to electrons was less than or equal to about 100. For such a large proportion of negative ions as 100:1, the inner-scale of turbulence-induced fluctuations in electron density at e.g. 70 km altitude should be about 600-1500 m, far longer than the 3 m needed to produce the radar echoes. Kirkwood et al. (2002a) therefore proposed that layers of charged aerosol particles must be involved in producing the radar echoes, either generating sharp gradients in electron density by scavenging electrons, or reducing the diffusivity of electrons through similar processes to those examined by e.g. Cho and Röttger (1997) and Hill et al. (1999) for the case of radar echoes from the summer mesopause. Kirkwood et al.'s (2002a) proposal that thin aerosol layers rather than turbulence cause PMWE found further support in the observation of extremely narrow layer widths (300 m or less), narrow spectral widths for the radar echo spectra and strong aspect sensitivity for the echoes.

In this paper we present quantitative comparisons of observed PMWE backscatter with turbulence theory, together with observations from a further solar-proton event which occurred during January 2002. On the latter occasion, both radar and lidar observations are available from the same location. We show that the lidar observations further support the proposal that aerosol particles are present in PMWE.

The ionospheric background during PMWE

Observations of PMWE during solar proton events offer the best possibilities to compare with the background ionospheric conditions. Measurements of the incoming

fluxes of solar protons are readily available (from the GOES satellites) and energy-dissipation / ion-chemistry models can be used to calculate background electron and ion densities (e.g. Kirkwood and Osepian, 1995). Calculated electron and ion densities are shown in Figure 1 for the event on 12/13 January 2002. The uppermost panel illustrates the proton fluxes. This is a rather weak solar proton event with fluxes barely above the instrument detection threshold which lies just below 10^{-1} proton cm^{-2} s^{-1} sr^{-1} . Model calculations for further events can be found in Kirkwood et al. (2002a,b). Since the proton fluxes during solar proton events generally vary rather slowly over a period of several days (after the initial onset) electron and ion production also vary slowly. The third panel in Figure 1 shows the model calculations of electron density based on the incoming proton fluxes. Above 75 km altitude, where negative ions are rare, the daily variation of electron density is small. Below 75 km altitude, there are few negative ions during daytime as negative ions are destroyed both by ultraviolet light and enhanced atomic oxygen, and the electron density remains high. In darkness, electrons attach easily to form negative ions, the ratio of number densities of negative ions to electrons, λ , becomes large, and the electron density falls. The fourth panel shows the ion-chemistry variations more explicitly in the form of the density of negative ions with the strong diurnal cycle in negative ion density. The final panel shows a comparison between observed cosmic noise absorption at 30 MHz, and that calculated from the model electron densities. This is discussed further in the next section.

Observations by ESRAD 52 MHz radar

The ESRAD radar is located at $67^{\circ} 53' \text{N}$, $21^{\circ} 06' \text{E}$. It is a 52 MHz radar operating, during these observations, with 72 kW of power and an antenna area of 2500 m^2 . For more details of the radar see Chilson et al. (1999). During January 2002 (and for most of the observations reported in Kirkwood et al., 2002a) observations were made in two modes, running in alternate 1-minute intervals. The first mode used an 8-bit complementary code with 600 m height resolution and covered heights 5-100 km. The second used uncoded pulses giving 300 m height resolution, covering heights 1 - 35 km and 60.5 – 80.5 km, with the latter aliased into the height interval 15-35 km. Observations using the 600 m mode are shown in Figure 1, which illustrates the observations on two consecutive days, 12 and 13 January 2002. Times are given as

decimal fractions of the UT day. The second panel shows the echo power detected by the 52 MHz ESRAD radar. Enhanced echo power, PMWE, is clearly seen during the hours around local noon (at 12.44 and 13.44 UT days).

The fifth panel illustrates the relationship between PMWE and λ , the ratio of negative ion to electron densities. The restriction of PMWE to times when $\lambda < 100$, can be seen clearly. The final panel shows a comparison with observed 30 MHz cosmic noise absorption and that calculated using the model. This parameter depends on the electron density in the height region of interest and illustrates that the proton fluxes (and the model calculation) do not account for all of the ionisation which must be present. It is likely that high-energy electrons also produce ionisation in this case, however there are no appropriate observations of incoming electrons which can be used to include them in the model. This means that the electron densities in the third panel may be underestimated by up to a factor 3-4. However, the value of λ varies little with electron density – it is primarily a function of height and solar zenith alone, so panel 5 still gives an accurate indication of the relation between PMWE and λ .

Comparison of radar backscatter with turbulence theory

Figure 2 shows a comparison of the observed radar backscatter cross sections with those expected on the basis of turbulence theory. Full details of the calculations are given in the Appendix. The backscatter levels for ESRAD observations reported in Kirkwood et al. (2002a) are shown as well as those for the event in Figure 1. These are plotted at the wavenumber ($k = 2\pi/l$) corresponding to a scale size (l) of 3 m.

There is also some evidence for similar scattering layers observed by the EISCAT VHF radar, corresponding to fluctuation scale-sizes (l) of about 70 cm (Collis et al., 1992 ; Kirkwood et al., 2002b). These are also marked. In both cases, the EISCAT data were obtained using the GEN-11 code (Turunen, 1986). Backscatter levels have been calculated as described in the Appendix - from the effective 'electron density' as published in Collis et al., 1992, and from 'raw electron densities' in EISCAT standard analyses in the NCAR CEDAR database (<http://cedarweb.hao.ucar.edu/>), for the event on 4 November 1997.

Calculations of the expected backscatter caused by layers of neutral turbulence are shown for a variety of conditions. Backscatter depends on a number of factors. The energy dissipation rate ϵ and the kinematic viscosity (which is a function of height) determine the inner-scale of neutral turbulent fluctuations. The ratio of negative ions to electrons (λ) determines the ratio between the inner-scales for electron density and for neutral turbulence. The atmospheric stability (parameterised by the Brunt-Väisälä frequency Ω_B), the electron density (N_e) and the electron density gradient determine the overall amplitude of electron-density fluctuations. The heavy black lines in Figure 2 represent conditions at 70 km altitude during weak solar proton events such as the one in Figure 1. The energy dissipation rate, 100 mW/kg is at the upper limit of the rates reported by Lübken (1993) during winter-time rocket flights. Dissipation rates 10 – 100 lower were reported to be more usual. The stability ($\Omega_B^2 = 4 \times 10^{-4} \text{ s}^{-2}$) is a typical model value, and is also the typical value found from the lidar temperature profile for 12/13 January 2002 as described below. The dashed lines (labelled “1a” and “3a”) show the effect of reducing the atmospheric stability to $\Omega_B^2 = 1 \times 10^{-4} \text{ s}^{-2}$, which represents an extreme case, as also described below. The dotted lines (labelled “2” and “4”) show the effect of increasing electron density by a factor 10, which corresponds to the most intense solar proton event when PMWE have so far been observed (9/10 November 2000, see Kirkwood et al., 2002a).

It is clear that turbulence theory might just be able to explain the weakest PMWE detected by ESRAD during sunlit conditions ($\lambda = 0$) during the most intense solar proton event. For all other conditions the observed radar backscatter is orders of magnitude above what can be expected due to neutral turbulence alone.

Observations by lidar

The University of Bonn Rayleigh-Mie-Raman backscatter lidar, based on a frequency doubled Nd:YAG laser (for details see Müller et al., 1997), is situated about 2 km away from ESRAD. The lidar detects light scattered both from atmospheric molecules and from aerosol particles, with the scatter cross-section per particle proportional to

the 6th power of the particle radius for small particles (up to 20 nm). During January 2002 data were recorded with a height resolution of 150 m and a temporal resolution of 250 s. The vertical lines in panel 2 of Figure 1 marks the beginning and end of the period, 14:50 UT on January 12th, to 02:10 UT on January 13th, when the lidar was able to make observations of adequate quality for mesospheric measurements (before and after this time interval the cloud cover was too much). Two alternative interpretations of the lidar backscatter profiles are possible. These are illustrated in Figures 3 and 4.

Alternative 1 – aerosol particles

Figure 3 illustrates the first of two possible alternative interpretations of the lidar profiles of backscattered light (integrated over the entire time interval of 10.5 hours). Here an observed signal enhancement above 70 km altitude is interpreted as caused by scattering material suspended in the atmosphere, i.e. as an increase of the backscatter ratio $R_L = \text{total signal} / \text{molecular signal}$. To estimate the molecular signal at 70 km altitude, we have fitted a low order polynomial to the range-corrected logarithm of the signal profile below (55 - 65 km) and above (75 – 85 km) the altitude with the suspected signal enhancement. The values interpolated by the polynomial in the altitude range 65 to 75 km were then taken as the molecular signal. R_L was calculated as the ratio between the received signal and the polynomial fit. This was done both with a high-resolution profile (the dashed line in the left-hand panel of Figure 3) and with the same smoothed profile which is used to determine a temperature profile in the next section (the solid line in the left-hand panel of Figure 3). An enhancement in backscatter ratio of up to about 1.1 centred at about 72 km can be clearly seen. To exclude the possibility that this result is an artefact of the way the data processing was performed, the degree of the interpolating polynomial has been varied as well as the fit ranges to as low as 50 km (limited by the stratopause) and as high as 105 km (limited by noise). While there are minor changes in the backscatter profile the basic structure of the signal enhancement remains the same. Further, the signal enhancement is visible above the noise, also in 30-minute-integrated subsets of data. This eliminates the possibility of electromagnetic interference (e.g. from switching of the thermostats of the electric heaters in the building) as a potential cause for the signal enhancement. Such interference could cause strong enhancement of the signal

recorded after occasional lidar pulses and give a spurious signal in a long integration, but would not appear consistently in all subsets.

The 2nd panel of Figure 3 shows the temperature profile corresponding to the smoothed background, and the solid line in the 3rd panel shows the buoyancy frequency (Ω_B) corresponding to this temperature profile. The dashed line shows an interpolated wind shear ($|du/dz|$, see “alt. 1” in Figure 5, for more details see below). In this interpretation of the lidar data the atmosphere is both statically stable ($\Omega_B > 0$) and dynamically stable ($\Omega_B > du/dz$) and no turbulence would be expected.

The right-hand panel of Figure 3 shows the maximum radar echo detected at each height on the 12th or 13th January. Clearly, both radar and lidar data (left-hand panel) show enhancements in the same height interval, from 65-75 km, taking into account that many hours of averaging are needed to determine the lidar profile. So, this first alternative interpretation of the lidar data (presence of aerosol particles) is consistent with the proposed role of aerosol particles in producing the radar echoes.

Alternative 2 – temperature inversion

Figure 4 shows the second of the two alternative interpretations of the lidar observations. In this case, the assumption is made that there are no aerosol particles present in the mesosphere. The height-profile of backscattered light is interpreted as due entirely to the density profile of the neutral atmosphere. Again we integrate the entire 10.5-hour period indicated in Figure 3. Using the hydrostatic assumption, the temperature profile can be calculated from the density profile (using the standard integral method for lidar data, initialising with a temperature value of 204.8 K at 79.76 km as according to MSIS90E (Hedin, 1991)). In this case a temperature inversion appears at 72 km altitude (2nd panel of figure 4). The 3rd panel of Figure 4 shows the profile of buoyancy frequency (Ω_B) calculated from lidar temperature profile. This indicates how the static stability varies with height due to the

temperature inversion. We note that, despite the rather deep temperature inversion, the atmosphere remains statically stable (buoyancy frequency above zero) at all heights.

We must consider whether this second alternative interpretation of the lidar data (no aerosol) might be the correct one. If the temperature inversion is due to a wave its amplitude is clearly large and it is apparently fairly stationary, i.e. it must persist at the same height throughout the several-hour averaging interval. Large temperature perturbations can, in principle, be created by gravity waves such as the stationary “mountain lee waves” which are not uncommon at the location of Esrang. Mountain lee waves in the mesosphere would be expected to arise when strong winds near the ground blow across the Scandinavian mountains and the winds at higher altitudes are in directions which allows further upward propagation. Similar waves might also be caused by a wind-jet in the upper troposphere, and would remain stationary as long as the jet remained at the same place. So the temperature structure in alternative 2 could in principle be real.

Next we consider whether an unusually strong turbulent layer is likely to have been present at the height where we observe the radar-echo layer. Figure 5 shows the wind speed and directions at our observation site and on the upwind-side of the Scandinavian mountains. The winds shown are for 12 UT on 12 and 13 January. Winds from the ground up to 55 km are available from UK meteorological office assimilations (UKMO) for both locations. At the radar site winds are available from the ESRAD 52 MHz MST radar for heights 2-11 km,, and from the Esrang SkiYmet meteor radar radar at heights 72-100 km . Between 55 and 70 km a wind profile has been interpolated, assuming a background windshear as defined by the UKMO winds at the lower limit and the SkiYmet winds at the upper limit. For alternative 1, a uniform shear has been assumed. For alternative 2, a wave has been superimposed on the background wind. This is the wave which would be consistent with the temperature perturbation in Figure 4 if it were caused by a mountain lee wave (see e.g Andrews, 2000).

The observations show that the wind is blowing from the north-west at heights up to 30 km, veering to south-westerly between 30 and 80 km altitude. Ground wind speeds are about 5 m/s on 12 January (10 m/s on 13 January) and wind speeds increase

strongly with altitude. These are conditions which generally can lead to upward-propagating lee-waves (see e.g. Réchou et al., 1999) and there are indeed signs of a wave in the lidar temperature and buoyancy-frequency profiles between 30 and 50 km altitude (not shown). It seems also that the winds would allow further upward propagation at least up to 80 km altitude. So a strong mountain lee-wave is a possible explanation for the proposed temperature inversion in Figure 4. There is also the possibility that the interaction between such orographically induced gravity waves and the stratospheric vortex edge/jet located close to our station might be the source of the disturbed temperature profile (see e.g. Whiteway et al., 1997; Duck et al., 2001).

As has been considered in previous studies (e.g. Thomas et al. 1996) a radar-echo layer due to enhanced turbulence from breaking (small-scale) gravity waves would be more likely to appear in the lower part of such a temperature inversion than in the upper part, since in the lower part the atmosphere is closest to static instability. Clearly (Figure 4) the stability is not reduced enough for static instability to lead directly to convective turbulence. For dynamic instability (i.e. turbulence generated by windshear) the onset condition is usually expressed in terms of the Richardson number ($Ri = \Omega_B^2 / (du/dz)^2$), where du/dz is the vertical shear of the horizontal wind. Turbulence is considered likely to arise if the Richardson number falls below 1/4. However, it is expected that turbulence, once initiated, can persist up to Richardson number = 1, which is the same as $\Omega_B = |du/dz|$. The dashed line in the 3rd panel of Figures 4 shows the term $|du/dz|$ for the interpolated winds (as labelled "alt 2" in Figure 5). The criterion for persistence of turbulence created by dynamic instability is reasonably satisfied between 65 and 71 km but not between 71 and 76 km. Of course, smaller-scale perturbations on the large-scale buoyancy and wind profiles might still lead locally to instability, but we would expect this to occur most readily where the large-scale stability (buoyancy frequency) is lower, i.e. between 65 – 71 km altitude. Comparing with the radar echo profile at the right-hand side of Figure 4, we see that enhanced echoes between 65 and 69 km correspond reasonably well with the height region where turbulence can be expected but the strongest radar echo, at 74 km is in a region which should not be experiencing turbulence.

The radar echoes are seen primarily during the day, whereas the lidar observations are from night, which makes an exact comparison difficult. However it can be seen in

Figure 1 that PMWE are generally present throughout the height interval 60-80 km and the strongest echoes appear above 72 km, which is inconsistent with expectations if the proposed temperature inversion persists through the hours before and after the lidar observations. Further, the short interval of PMWE within the lidar integration period (UT day 12.6 –12.8) is found between 72 and 75 km altitude, i.e. in the most stable part of the proposed temperature inversion. This is not consistent with the expectations outlined above.

So, the second alternative interpretation of the lidar observations, a deep temperature inversion, can explain the presence of turbulence at the same height as PMWE layers between 65 and 70 km, but not at the height of the PMWE layers above and below this region. Added to this, the turbulence between 65 and 70 km would have to be several orders of magnitude stronger than any observed in the numerous sounding-rocket experiments reported by Lübken (1993), Lübken et al. (1993) and Lübken (1997) if it were to produce significant fluctuations at the 3 m scale needed to generate echoes for our 50 MHz radar (see Figure 2).

Discussion and Conclusions

We have presented two alternative interpretations of joint radar and lidar observations of enhanced radar-echo layers in the winter, high-latitude mesosphere (PMWE).

If “alternative 1” (Figure 3) represents the correct interpretation of the lidar observations, we can speculate that charged aerosol particles are gathered into layers by dynamic effects causing steep gradients in electron density. Such gradients can cause enhanced radar echoes without the presence of turbulence. The disappearance of PMWE as λ increases above ~ 100 can be accounted for by considering the relative rates of capture by aerosol particles of ions and electrons. At $\lambda \sim 100$ the rates become approximately equal (Kirkwood et al., 2002a). At higher values of λ aerosol particles should scavenge negative ions rather than electrons, leaving the electrons free to diffuse rapidly, removing any gradient in electron density.

If “alternative 2” (Figure 4) represents the correct interpretation of the lidar observations, we can speculate that some, but not all, PMWE layers are associated with turbulence. However, as we have shown in Figure 2, turbulence alone cannot account for the strength of the radar echoes unless some agent (such as charged aerosol particles) reduces the attenuation of turbulent fluctuations at small scale sizes. In order to explain the disappearance of PMWE as λ increases above ~ 100 , agents which decrease diffusivity by a factor more than 100 are needed. Even in alternative 2, the evidence suggests that PMWE can also occur at heights where turbulence is not expected. In this case they can be explained in the same way as in alternative 1. Note that “alternative 2” assumes that no aerosol particles are visible to the lidar. This is not necessarily a contradiction since the aerosol particles may simply be too small to cause detectable enhanced backscatter at the lidar wavelength.

PMWE have been observed by radar on several occasions (Kirkwood et al., 2002a) whereas simultaneous lidar observations have so far been obtained on only one occasion, the one reported here. Our radar detections of PMWE have all been made during wintertime solar proton events. We cannot rule out the possibility that such layers are present at other times or at other latitudes. Without the high levels of ionisation produced by the solar protons, the layers would not be detectable by our radar, nor by similar radars at other locations. However, there have been a number reports (Ecklund and Balsley, 1981, Balsley et al., 1983, Czechowsky et al., 1989) from other, more powerful radars of echoing layers in the winter mesosphere during periods of generally enhanced ionisation (i.e due to energetic auroral electrons). Previously, explanations of these in terms of neutral turbulence have been proposed. However, more recent direct measurements (by sounding rockets) of the characteristics of turbulent layers (Lübken et al. 1993; Lübken 1993, 1997) show that fluctuations with the scale sizes needed to produce the radar echoes are very strongly attenuated in the neutral turbulence. The only known way to extend the scale sizes of turbulence in the electron gas to substantially shorter scale-sizes than those in the neutral gas is through the presence of charged aerosol particles or massive ions (e.g. Cho and Röttger, 1997, Hill et al., 1999).

If aerosol layers were widely present in the mesosphere it might be expected that they would be seen by lidar, at least on those occasions when aerosol particles grew to sufficient size. However, the normal assumption used in interpreting lidar backscatter profiles from the winter mesosphere is that there are no aerosol particles present. Any small perturbations due to aerosol layers will generally be interpreted as waves or “inversions” in the temperature profile. In general, the wave activity (gravity waves, planetary waves and tides) in the winter mesosphere is at a rather high level and waves in temperature profiles would be considered normal. The amplitude of the wave or temperature inversion needed to explain the lidar backscatter profile on 12/13 January 2002 is about 20 K peak-to-peak, larger than most of those reported from the ALOMAR lidar site at nearby Andøya (Fiedler et al., 1999). However, at least one similar amplitude wave can be seen in Fiedler et al.'s profiles for October 1998, which could, in principle, have been an aerosol layer rather than a true temperature wave.

Large temperature inversions at mid and low-latitudes, derived from lidar backscatter observations under the aerosol-free assumption, have been reported by several authors (Hauchecorne et al., 1987, Whiteway et al., 1995, Leblanc and Hauchecorne, 1997, Meriwether and Gardner., 2000, Sica et al., 2002), sometimes related to radar-echo layers (Thomas et al., 1996, Ratnam et al., 2002). In a few cases, the lidar – derived temperature inversion has been seen by independent measurements (e.g. by satellite remote sensing, Leblanc and Hauchecorne, 1997). Indeed the first report of a mesospheric temperature inversion was from falling-sphere measurements, which are not dependent on the no-aerosol assumption (Schmidlin, 1976). So it seems clear that substantial and persistent temperature inversions can sometimes occur in the mesosphere. However it remains possible that some mesospheric “temperature inversions” derived entirely on the basis of lidar backscatter profiles may be misinterpretations of weak aerosol layers.

The only possibility to discriminate between artefacts of the no-aerosol assumption and true temperature waves is to compare temperatures derived from lidar measurements with independent measurements such as by falling sphere, at the same place and time. In a careful comparison by Lübken et al. (1994) a discrepancy was indeed found between lidar and falling sphere densities at heights 75-90 km for a

number of winter measurements at Biscarosse (44°N, 1°W). Lübken et al. considered the possibility that aerosol particles were affecting the lidar backscatter and found that this was a reasonable explanation, and that the aerosol particles could correspond to the “meteoric smoke” proposed by Hunten et al. (1980), provided the particle sizes were around 6-7 nm or more.

It is generally accepted that the well known aerosol layers at the summer mesopause (noctilucent clouds) and in the winter lower stratosphere (polar stratospheric clouds) are largely composed of water, which condenses/freezes out of the atmosphere at the very low temperatures prevailing at these locations (ca 140 K and 190 K, respectively). Temperatures in the winter mesosphere are much higher, far above those needed for water-saturation. A possible source of aerosol particles is ablation and recondensation of meteoric material (which includes meteoric “dust” as proposed by Hunten et al., 1980 but could also include ablated material from space debris).

It is worthwhile to consider how much the meteoric dust distribution proposed by Hunten et al. (1980) would have to be modified to be able to explain the present lidar observations. Table 1 compares backscatter calculated for the aerosol particle size/density distributions given in Hunten et al. (1980) with backscatter expected from atmospheric molecules at 60 km and 90 km respectively. The aerosol distribution predicted by Hunten et al. changes rapidly between 90 and 80 km but more slowly towards lower heights, so that the results for 60 km are likely to be more representative of conditions at the height of our observations (65-75 km). Note that, although the number density of particles decreases by an order of magnitude between 90 km and 60 km, the particles are becoming larger as they sediment and this dominates the effect on the aerosol backscatter. Table 1 suggests that a backscatter ratio of about 1×10^{-4} should be expected at 65-75 km if meteoric dust/smoke is present with the size/density characteristics predicted by Hunten et al.’s model. Clearly this is several orders of magnitude less than we have observed, which is about 1×10^{-1} (Fig. 3). In order to achieve such a high backscatter ratio, the aerosol particles would have to be present in greater numbers (backscatter proportional to number density) or with larger sizes than in the model (backscatter proportional to the 6th power of the radius, i.e. r^6 , so long as r is much less than the lidar wavelength). One possible explanation

for our observations could be that dynamic processes concentrate particles into a layer with 1000 times the modelled number density. However this is a huge redistribution and a more likely explanation would be that the particles are slightly larger than as modelled by Hunten et al. In this case, it must be remembered that the total amount of material available for particle formation is limited by the meteor flux into the atmosphere and the mass of each particle is proportional to r^3 . So increasing particle size necessarily leads to lower numbers of particles, by a factor r^{-3} . Given this constraint, if the particle size is assumed to increase by a factor 5 for example, the number of particles will change by a factor 5^{-3} . The total backscatter will change by a factor of $5^6 \times 5^{-3}$, i.e. 125. To explain our observations, there then remains a need for a further factor 8 to be contributed by redistribution of the particles into a concentrated layer.

There is considerable uncertainty regarding the amount of meteoric material entering the system from above. Hunten et al.'s calculations are based on an estimate of 44×10^3 kg/day whereas higher fluxes about 100×10^3 kg/day have been suggested by observations above the atmosphere by the Long Duration Exposure Facility (Love and Brownlee, 1993). On the other hand, Mathews et al. (2001) have argued, on the basis of radar measurements, that fluxes are much lower, around 10×10^3 kg/day. So the layer concentration factor described above could lie between 4 and 40. Our observations clearly indicate aerosol particles in a distinct layer and would be consistent with concentration factors in this range.

Regarding the possibility of larger aerosol particles than modelled by Hunten et al., we note that the processes of aerosol-particle growth in the atmosphere are generally poorly understood, even at heights where direct measurements are readily available. Many new ideas have been introduced since the Hunten et al (1981) paper. For example, the latter authors assumed only coagulation of uncharged particles, arguing that particle charging would reduce coagulation. Newer results suggest that particle charge can enhanced rather than hinder aerosol-particle growth in the atmosphere including in the stratosphere and mesosphere (Yu and Turco, 2000, Nadykto and Yu, 2003).

There is already compelling evidence that aerosol-particle layers can occur in the polar upper stratosphere, apparently in contradiction with accepted ideas regarding chemistry and aerosol formation (Gerding et al., 2003). The layer reported in the latter paper occurred in the same season and at the same location (among others) as the observations we present here. It produced depolarisation of backscattered light demonstrating that it was composed of aspherical, i.e. solid particles. It appeared first at 38 km altitude and descended over a three-month period to 25 km, i.e. rather lower heights than the present observations. It should be noted that we would not expect to observe radar echoes from a layer at such low altitude because of the lack of sufficient ionisation. However, Gerding et al.'s aerosol layer may well have a similar origin to the particle layers which seem to be candidates for enhanced radar echoes (PMWE) at higher altitudes.

Clearly an unequivocal demonstration that PMWE correspond to aerosol layers requires further observations. Simultaneous profiling with lidar and falling-spheres during a PMWE event are probably the best available test. However, the evidence presented here and by Kirkwood et al. (2002a) is strong enough to raise serious questions as to the accuracy of the widespread assumption that aerosol particles in the winter mesosphere are too few and too small to have a significant influence on radar or lidar scatter.

Acknowledgements

The ESRAD MST radar is operated jointly by Swedish Institute of Space Physics and Swedish Space Corporation, Esrange. The University of Bonn lidar was operated under grant 50EE0009 from DLR Erdbeobachtung, Germany. Riometer data from Abisko were provided by Sodankylä Geophysical Institute, Finland. This research has largely been funded by the Swedish Science Research Council.

Appendix

Calculation of observed radar backscatter

The volume reflectivity of the atmospheric scatterers $\eta(k)$ can be determined by radar using observations of the ratio of received and transmitted powers and information on the properties of the radar and the volume contributing to the scatter. For any given radar wavelength λ_{radar} , the volume reflectivity obtained will be that at the wave-number $k = 4\pi / \lambda_{radar}$. The appropriate relationship can be expressed as

$$\eta(k) = \frac{P_r}{P_t} \frac{64(2\ln 2)r^2}{\pi L A_e F \Delta r} \quad (1)$$

where P_t and P_r are transmitted and received power, respectively, r is the distance to the scattering volume, Δr is the thickness of the volume element along the radar beam, A_e is the effective area of the receiving antenna, L is an efficiency factor (<1) and F expresses the fraction of the scattering volume which is filled with scatterers (Gage, 1990, note that the same equation appears in many papers with slightly different values of numerical constants. The differences (up to 20%) are due to slightly different assumptions on the shape of the radar beam and on the definition of effective area of the antenna, for a discussion see e.g. Röttger and Larsen, 1990, Sato 1989).

Note that, in the estimates of η made here from the ESRAD observations, L and F have been assumed to be 1 and A_e has been taken as the full area of the antenna receiving segment, so η is likely to be somewhat underestimated.

The power received by the radar can be estimated by comparing the signal level with background noise (for ESRAD), or with some calibration noise signal (typically for EISCAT).

$$P_r = k_b B T_n (SNR) \quad (2)$$

where k_b is Boltzman's constant (JK^{-1}), B is the receiver bandwidth (Hz), T the temperature of the noise source (K) and the signal to noise ratio SNR is dimensionless (see e.g. Baron, 1977). Note that SNR in this equation denotes the ratio of the signal power returned by the atmospheric scatterers to the signal power detected in the receiver due to the respective reference noise source, for a single transmitted radar pulse. In the case of MST radar such as ESRAD signal amplitudes are usually integrated from a large number (m) of transmitted pulses. In the integrated result, the power returned by (coherent) atmospheric scatterers is increased by a factor m^2 while the power due to (random) noise is increased by a factor m . This must be taken into account in applying eq. 2. For incoherent-scatter radars such as EISCAT, it is generally signal power which is integrated, rather than amplitude so that both atmospheric scatter and noise powers are increased by the same factor m .

The reference noise source which is available for ESRAD is the background noise, i.e. the incoming signal power averaged over altitudes where no atmospheric scatterers are present. This comprises internal system noise plus galactic radio noise. According to the radio-sky survey by Maeda et al. (1999), the galactic noise at ESRAD's latitude and frequency should vary over the siderial day between about 4500 K and 12000 K. This variation is recorded in the ESRAD data and provides a reference by which the total background noise temperature can be determined.

For the EISCAT radar an injection noise source is used for applying eq. 2 and A_e and L in eq. 1 are found by comparing measured P_r with theoretical expectations for the scatter from ionospheric plasma, on occasions when the plasma density can be determined by independent methods, such as ionosondes (see e.g. Evans, 1969, Kirkwood et al., 1986). This calibration is incorporated into standard data analysis procedures which calculate 'raw electron density', N_e^* which is simply the number density of electrons (or ions) which would produce the observed scattered power, with the assumption that the scattering volume is uniformly filled and that the effective scatter cross section σ_e per electron is $4.99 \times 10^{-29} \text{ m}^2$. Rearranging the radar equation for incoherent scatter (Evans, 1969, eq. 28) and substituting the parameters as we have defined them above gives :

$$N_e^* \sigma_e = \frac{P_r}{P_t} \frac{8\pi r^2}{0.76LA_e \Delta r}$$

This is very similar to eq. 1, differing only by ca. 20% in the values of the numerical constants (due to different assumptions on antenna characteristics) and by the lack of the volume filling factor F . So we can find the volume reflectivity for EISCAT observations as :

$$\eta(k) = N_e^* \cdot \sigma_e / F \quad (3)$$

In the estimates of η made here from the EISCAT observations, F has been assumed to be 1, so η may be underestimated.

Calculation of expected radar backscatter from turbulence

Many theoretical and laboratory studies of the characteristics of turbulence in different conditions have been made. Recent theoretical studies of particular relevance for the middle atmosphere have been published by Driscoll and Kennedy (1985) and Hill et al. (1999). The most relevant experimental studies are the series of sounding-rocket flights reported by Lübken (1993). Lübken's work involved direct measurements of the scale-size spectrum of neutral density fluctuations in the high-latitude mesosphere, during both summer and winter. Lübken found close correspondence between observations and two alternative theoretical models, named according to their authors, Heisenberg (1948) and Tatarskii (1961). Since the Heisenberg model predicts slightly higher fluctuation levels at short scale sizes than the Tatarskii model, we here adopt the Heisenberg model. Lübken used the one dimensional form of the scale-size spectrum, which is appropriate for a rocket-borne probe travelling through the turbulent medium. The wave-number spectrum of turbulent fluctuations of a suitable tracer, in this case neutral density fluctuations, is :

$$W(k) = P \frac{k^{-5/3}}{(1 + \{k/k_o\}^{8/3})^2} \quad (4)$$

Where P is a constant which depends on the turbulent energy dissipation rate, the properties of the atmosphere and the nature of the 'tracer' of the turbulence. The value of $k_o = 2\pi/l_o$, where l_o is the 'inner scale size' at which the turbulence passes from the 'inertial' to the 'viscous' subrange. The limiting cases are $W(k)$ proportional to $k^{-5/3}$ as k tends to zero, and $W(k)$ proportional to k^{-7} as k tends to infinity. Lübken determined values of l_o (and hence k_o) by fitting the spectral form in (4) to observed turbulent fluctuations of neutral density. From k_o the turbulent energy dissipation rates ε were estimated from :

$$\varepsilon = \left[\frac{9\Gamma(\frac{5}{3})\sin(\frac{\pi}{3})f_\alpha a^2 \nu}{16P_r} \right]^3 k_o^4 \quad (5)$$

Here, f_α and a^2 are factors determined from experiments, observations and numerical models. Commonly used values are 1 and 2.8 (e.g. Hocking, 1985). However, Lübken (1993) used values 2 and 1.74, obtained from a review of observations by Hill (1978b). The Prandtl number P_r is the ratio of molecular diffusion (D_m) to kinematic viscosity (ν) and Lübken (1993) used a value of $P_r = 0.83$. In order to ensure that our estimates of turbulent radar-scatter are based on the best experimental evidence of the scale-size distribution the turbulence in the relevant conditions, we adopt the same relation as Lübken between ε and k_o .

When we consider the radar backscatter we must use the three-dimensional form of (4) since the radar is sensitive only to fluctuations which have their k vector parallel to the radar beam, i.e. $Y(k)$ proportional to $W(k)/k^2$ (Hocking, 1985) The scale-size distribution for a suitable tracer can then be written as :

$$Y(k) = R \frac{k^{-11/3}}{(1 + \{k/k_o\}^{8/3})^2} \quad (6)$$

The 'tracer' in this case is fluctuations in refractive index, which depend on fluctuations in electron density. Since the refractive index depends not only on the electron density fluctuations themselves but also on the wavelength of the probing radar, R is now a function of k ($=4\pi/\lambda_R$, where λ_R is the radar wavelength).

In the case when the ionospheric plasma consists of positively charged molecular ions and electrons only, the electron diffusion is controlled by the ions (ambipolar diffusion). The ion diffusion is essentially the same as the molecular diffusion and k_o can be calculated using (5). In the case when the ionospheric plasma consists of both negatively and positively charged ions with similar diffusivities, together with electrons, the electron diffusion increases by a factor $(1 + \lambda)$, where λ is the ratio of negative ions to electrons (Hill, 1978a). This is equivalent to decreasing the Schmidt number S_c by a factor $(1 + \lambda)$, where S_c is the ratio of kinematic viscosity (ν) to electron diffusion (D_e). There is now an inertial-diffusive subrange introduced in the turbulence in which the one-dimensional spectrum follows approximately a $k^{-17/3}$ form instead of the k^{-7} form appropriate for the viscous subrange (Driscoll and Kennedy, 1985). The transition from inertial to inertial-diffusive behaviour occurs at $k_c \approx S_c^{3/4} k_o$. In the case $S_c > 1$ we assume the spectral form :

$$Y'(k) = R \frac{k^{-17/3}}{(1 + \{k/k_c\}^{6/3})^2} \quad (7)$$

Following Hocking (1985, eqs 3,4,37) the factor R in equation (6) or (7) can be found from

$$R = 0.033 f_\alpha a^2 M_e^2 \epsilon^{2/3} Ri \Omega_B^{-2} \quad (8)$$

where Ω_B is the buoyancy frequency in the atmosphere and Ri is the gradient Richardson number which should be less than 1/4 at the onset of turbulence but which can increase to about 1 before turbulence ceases. M_e is the potential refractive index which is given by Hocking (1985, equation 21) :

$$M_e = \frac{2\pi r_e}{k^2} \left[N_e \frac{\Omega_B^2}{g} - \frac{dN_e}{dz} - (1.4 \times 10^{-4}) N_e \right] \quad (9)$$

where N_e is electron density, r_e the classical electron radius (2.8×10^{-15} m).

The radar backscatter is then (Hocking 1985, eqs 25-29)

$$\eta(k) = 2\pi^2 k^4 Y(k) \quad (10)$$

We want to calculate the highest likely radar backscatter from neutral turbulence. So we adopt f_a and a^2 as 2 and 1.72, respectively, as in Lübken (1993). We take $\varepsilon = 100$ mW/kg which is the upper limit of energy dissipation rates found by Lübken (1993) for thin layers in the winter mesosphere and we assume $Ri = 1$. We perform the calculations for a representative height of 70 km (which defines $\nu = 0.247 \text{ m}^2\text{s}^{-1}$ according to the MSIS90E model of Hedin, 1991). Electron densities are taken from model results for typical solar proton events such as the one in Figure 1, and for the strongest event during which PMWE have been observed (Kirkwood et al., 2002a). Atmospheric buoyancy frequency is taken as $\Omega_B = 2 \times 10^{-2} \text{ s}^{-1}$ or $1 \times 10^{-2} \text{ s}^{-1}$. The former is a typical value for an undisturbed upper mesosphere as can be seen in Figure 3. The latter value corresponds to a possible less-stable state as illustrated by Figure 4.

References

Andrews, D.G., 2000. *An Introduction to Atmospheric Physics*, pp133-137, Cambridge University Press, Cambridge, England.

Balsley, B.B., Ecklund, W. L., Fritts, D. C. , 1983. VHF echoes from the high-latitude mesosphere and lower thermosphere: observations and interpretations, *J. Atmos. Sci.* 40, 2451-2466.

Baron, M., *The Chatanika radar system, 1977*. In : *Radar probing of the auroral plasma*, ed. A. Brekke, Universitetsforlaget, Oslo, 103-141.

Chilson, P., Kirkwood, S., Nilsson, A., 1999. The Esrange MST radar: a brief introduction and procedure for range validation using balloons, *Radio Sci.* 34, 427-436.

Cho, J., Röttger, J., 1997. An updated review of polar mesosphere summer echoes: Observations, theory, and their relationship to noctilucent clouds and subvisible aerosols, *J. Geophys. Res.* 102, 2001-2020.

Collis, P.N., Rietveld, M.T., Röttger, J., Hocking, W.K., 1992. Turbulence scattering layers in the middle-mesosphere observed by the EISCAT 224-MHz radar, *Radio Sci.* 27(2), 97-107.

Czechowsky, P., Reid, I.M., Rüster, R., Schmidt, G., 1989. VHF radar echoes observed in the summer and winter polar mesosphere over Andøya, Norway, *J. Geophys. Res.* 94, 5199-5217.

Driscoll, R., Kennedy, L. A., 1985. A model for the spectrum of passive scalars in an isotropic turbulence field, *Phys. Fluids*, 28, 72 - 80.

Duck, T.J, Whiteway, J.A., Carswell, A.I. , 2001. The gravity wave - Arctic stratosphere vortex interaction, *J. Atmos. Sci.* 58, 3581 – 3596.

- Ecklund, W. L., Balsley, B. B., 1981. Long-term observations of the Arctic mesosphere with the MST radar at Poker Flat, Alaska, *J. Geophys. Res.* 86, 7775-7780.
- Evans, J.V., 1969. Theory and practice of ionosphere study by Thomson scatter radar, *Proc. IEEE*, 57, 496-530.
- Fiedler, J., von Cossart, G., von Zahn, U., Eriksen, W., 1999. Stratospheric/mesospheric temperature profiles obtained by ALOMAR RMR lidar over Andøya, *Proc. 14th ESA Symposium on European Rocket and Balloon Programmes and Related Research*, ESA SP-437, 263-268.
- Gage, K., 1990. Radar observations of the free atmosphere, In : Atlas D. (Ed.), *Radar in Meteorology* (ch. 28a). American Meteorological Society.
- Gerding, M., G. Baumgarten, U. Blum, J.P. Thayer, K.-H. Fricke, R. Neuber and J. Fiedler, 2003. Observation of an unusual mid-stratospheric aerosol layer in the Arctic : possible sources and implications for polar vortex dynamics, *Ann. Geophys.* 21, 1057-1069.
- Hauchecorne, A., Chanin, M.L. , Wilson, R. , 1987. Mesospheric temperature inversion and gravity wave breaking, *Geophys. Res. Lett.* 14, 933-936.
- Hedin, A. E., 1991. Extension of the MSIS thermosphere model into the middle and lower atmosphere, *J. Geophys. Res.* 96, 1159-1172.
- Heisenberg, W., 1948. Zur statistischen Theorie der Turbulenz, *Z. Physik* 124, 628-657.
- Hill, R.J., 1978a. Nonneutral and quasi-neutral diffusion of weakly ionized multiconstituent plasma, *J. Geophys. Res.*, 83, 989-998.
- Hill, R.J., 1978b. Models of the scalar spectrum for turbulent advection, *J. Fluid Mech.* 88, 541-562.

Hill, R.J., Gibson-Wilde, D.E., Werne, J.A., Fritts, D.C., 1999. Turbulent induced fluctuations in ionisation and application to PMSE, *Earth Planets Space* 51, 499-513.

Hocking, W.K., 1985. Measurement of turbulent energy dissipation rates in the middle atmosphere by radar techniques : A review, *Radio Sci.* 20 (6), 1403-1422.

Hunten, D. M., Turco, R. P., Toon, O. B., 1981. Smoke and dust particles of meteoric origin in the mesosphere and thermosphere, *J. Atmos. Sci.* 37, 1342-1357.

Kirkwood, S., Collis, P.N., Schmidt, W., 1986. Calibration of electron densities for the EISCAT UHF radar, *J. Atmos. Terr. Phys.* 48, 773-775.

Kirkwood, S., Osepian, A., 1995. Quantitative studies of energetic particle precipitation using incoherent-scatter radar, *J. Geomagn. Geoelectr.* 47, 783-799.

Kirkwood S., Barabash, V., Belova, E., Nilsson, H., Rao, T. N., Stebel, K., Osepian, A., Chilson, P. B., 2002a. Polar mesosphere winter echoes during solar proton events, *Advances in Polar Upper Atmosphere Research* 16, 111-125.

Kirkwood S., Barabash, V., Belova, E., Nilsson, H., Rao, T. N., Stebel, K., Blum, U., Fricke, K.-H., Osepian, A., Chilson, P. B., 2002b. Polar Mesosphere Winter Echoes - by ESRAD, EISCAT and lidar, *memoirs of the British Astronomical Association* 45, paper 07, editors. M. Gadsden and N. James

Leblanc, T., Hauchecorne, A., 1997. Recent observations of mesospheric temperature inversions, *J. Geophys. Res.* 102, 19471-19482.

Love, S.G., and D.E. Brownlee, 1993. A direct measurement of the terrestrial mass accretion rate of cosmic dust, *Science*, 262, 550- 553.

Lübken, F. J., 1993. Experimental results on the role of turbulence for the heat budget of the upper atmosphere, Bonn University report BONN-IR-93-51, Bonn, Germany.

Lübken, F.-J., 1997. Seasonal variation of turbulent energy dissipation rates at high latitudes as determined by in situ measurements of neutral density fluctuations, *J. Geophys. Res.*102, 13441-13456.

Lübken, F.-J., Hillert, W., Lehmacher, G., von Zahn, U., 1993. Experiments revealing small impact of turbulence on the energy budget of the mesosphere and lower thermosphere, *J. Geophys. Res.* 98, 20369 - 20384.

Lübken, F.-J., Hillert, W., Lehmacher, G., von Zahn, U., Bittner, M., Offerman, D., Schmidlin, F., Hauchecorne, A., Mourier, M., Czechowsky, P., 1994. Intercomparison of density and temperature profiles obtained by lidar, ionization gauges, falling spheres, datasondes and radiosondes during the DYANA campaign, *J. Atmos. Terr. Phys.* 56, 1969-1984.

Maeda, K., Alvarez, H., Aparici, J., May, J., Reich, P., 1999. A 45-MHz continuum survey of the northern hemisphere, *Astron. Astrophys. Suppl. Ser.* 140, 145-154.

Mathews, J.D., D. Janches, D. D. Meisel, and Q.-H. Zhou, 2001. The micrometeoroid mass flux into the upper atmosphere: Arecibo results and a comparison with prior estimates. *Geophys. Res. Lett.*, 28, (10), 1929-1932.

Meriwether, J.W., Gardner, C.S., 2000. A review of the mesosphere inversion layer phenomenon, *J. Geophys. Res.*105, 12405-12416.

Müller, K.P., Baumgarten, G., Siebert, J., Fricke, K.H., 1997. The new lidar facility at Esrange, Kiruna, Proc.13th ESA Symposium on European Rocket and Balloon Programmes and Related Research, ESA-SP-397, 129-134.

Nadykto Alexey B. and Fangqun Yu, 2003. Uptake of neutral polar vapor molecules by charged clusters/particles: Enhancement due to dipole-charge interaction. *J. Geophys. Res.* 108 (D23) 4717, doi:10.1029/2003JD003664.

Ratnam V. M., Rao, D. N., Rao, T. N., Kumar, Y. B., Kumar, V. S., Rao, P.B., 2002. Coordinated MST radar and lidar observations for the study of mesospheric structures over a tropical station, *J. Atmos. Sol. Terr. Phys.* 64, 349-358.

Réchou, A., Barabash, V., Chilson, P., Kirkwood, S., Savitskaia, T., Stebel, K. , 1999. Mountain wave motions determined by the Esrange MST radar, *Ann. Geophys.* 17, 957 - 970.

Röttger, J., Larsen, M.F., 1990. UHF/VHF radar techniques for atmospheric research and wind profiler applications, In: Atlas, D., (Ed.), *Radar in Meteorology*. American Meteorological Society.

Sato, T., 1989. Radar principles, In: Fukao, S., (Ed.), *Middle Atmosphere Program, Handbook for MAP, Vol 30 (International School on Atmospheric Radar)*, SCOSTEP.

Schmidlin, F. J., 1976. Temperature inversion near 75 km, *Geophys. Res. Lett.* 3, 173-176.

Sica , R.J., Thayaparan, T., Argall, P.S., Russell, A.T., Hocking, W.K. , 2002. Modulation of upper mesospheric temperature inversions due to tidal-gravity wave interactions, *J. Atmos. Sol. Ter. Phys.* 64, 915-922.

Tatarskii, V.I., 1961. *Wave propagation in a turbulent medium*, McGraw-Hill Book Company, New York.

Thomas, L., Marsh, A.K.P., Wareing, D.P., Astin, I., Chandra, H., 1996. VHF echoes from the mid-latitude mesosphere and the thermal structure observed by lidar, *J. Geophys. Res.* 101, 12867-12877.

Thrane, E.V., Grandal, B., 1981. Observations of fine-scale structure in the mesosphere and lower thermosphere, *J. Atmos. Terr. Phys.* 43, 179-189.

Turunen, T., 1986. GEN-SYSTEM – A new experimental philosophy for EISCAT radars, *J. Atmos. Terr. Phys.* 48, 777-785.

Whiteway J.A., Carswell, A.I., Ward, W.E., 1995. Mesospheric temperature inversions with overlying nearly adiabatic lapse rate: an indication of a well-mixed turbulent layer, *Geophys. Res. Lett.* 22, 1201-1204.

Whiteway J.A., Durck, T.D., Donovan, D.P., Bird, J.C., Pal, S.R., Carswell, A.I., 1997. Measurements of gravity wave activity within and around the Arctic stratospheric vortex, *Geophys. Res. Lett.* 24, 1387-1390

Yu, F., and R. P. Turco, 2000. Ultrafine aerosol formation via ion-mediated nucleation, *Geophys. Res. Lett.*, 27, 883– 886.

Table 1. Calculated backscatter coefficients for air molecules and for aerosol particle distributions in Hunten et al. (1981) assuming refractive index $(1.67 + 0.01i)$ and lidar wavelength 532 nm.

Quantity	60 km	90 km	units
Aerosol particles number density	1.8×10^3	6.8×10^4	cm^{-3}
backscatter coefficient	6.5×10^{-16}	8.6×10^{-19}	$\text{cm}^{-1}\text{sr}^{-1}$
max backscatter occurs at particle radius	10	2.6	nm
Molecules number density	6.8×10^{15}	8.3×10^{13}	cm^{-3}
backscatter coefficient	4.2×10^{-12}	5.1×10^{-14}	$\text{cm}^{-1}\text{sr}^{-1}$
Backscatter Ratio (aerosol particles / molecules)	1.5×10^{-4}	1.7×10^{-5}	

Figure 1 – ESRAD data and model results for 12/13 January 2002. Panel 1: Proton fluxes measured at geostationary orbit (normal undisturbed level is shown by the horizontal dotted line). Panel 2: Signal and noise power detected by the radar, the background (noise) level is 15 dB (white) and the strongest signals exceed 25 dB (black). Vertical lines on the second panel indicate the start and end of the lidar data-integration period. Panel 3: Electron densities calculated from the proton flux measured by GOES (units cm^{-3}). Panel 4: Calculated negative ion densities (units cm^{-3}). Panel 5: Contours of the ratio of negative ion density to electron density (λ) overlaid with circles indicating times and heights when and where PMWE were detected. Panel 6: Cosmic-noise absorption calculated from the electron densities in the third panel (circles) and absorption measured by the riometer at Abisko, 100 km west of ESRAD.

Figure 2. Radar volume reflectivities estimated from radar observations (ESRAD as bars, EISCAT as dots, dates in form YYMMDD) and from turbulence theory (lines). Dates of radar observations are indicated. Calculations from turbulence theory are described in the Appendix. Curve 1 corresponds to electron density $N_e = 3 \times 10^8 \text{ m}^{-3}$, electron-density gradient $dN_e/dz = 9 \times 10^4 \text{ m}^{-4}$, square of Brunt-Väisälä frequency $\Omega_B^2 = 4 \times 10^{-4} \text{ s}^{-2}$; Curve 1a as curve 1 but $\Omega_B^2 = 1 \times 10^{-4} \text{ s}^{-2}$; Curve 2 is for $N_e = 3 \times 10^9 \text{ m}^{-3}$, $dN_e/dz = 9 \times 10^5 \text{ m}^{-4}$, $\Omega_B^2 = 4 \times 10^{-4} \text{ s}^{-2}$; Curve 3 corresponds to $N_e = 3 \times 10^9 \text{ m}^{-3}$, $dN_e/dz = 9 \times 10^4 \text{ m}^{-4}$, $\Omega_B^2 = 4 \times 10^{-4} \text{ s}^{-2}$; Curve 3a as curve 3 but $\Omega_B^2 = 1 \times 10^{-4} \text{ s}^{-2}$; Curve 4 is for $N_e = 3 \times 10^{10} \text{ m}^{-3}$, $dN_e/dz = 9 \times 10^5 \text{ m}^{-4}$, $\Omega_B^2 = 4 \times 10^{-4} \text{ s}^{-2}$. Curves 1, 1a and 2 for dawn/dusk conditions when there are 100 times as many negative ions as free electrons ($\lambda=100$). Curves 3, 3a and 4 for midday conditions with no negative ions ($\lambda=0$). All curves for energy dissipation rate $\epsilon = 100 \text{ mW/kg}$, and for height 70 km.

Figure 3 . Panel 1: Lidar backscatter ratio for the interval between 14.50 UT on 12 January 2002 and 02.10 UT on 13 January 2002, assuming a smooth neutral density profile (see text for details). Height resolution is 150 m. Panel 2: Temperature profile corresponding to the smooth neutral density profile. Panel 3: Buoyancy frequency from the temperature profile in the second panel (solid line) and windshear from winds in Figure 5 "alt. 1" (dotted line). Panel 4: Maximum radar echo power detected

between 0 UT on 12 January 2002 and 24 UT on 13 January 2002 (arbitrary units). Height resolution is 600 m. Dashed line indicates the noise level.

Figure 4. Panel 1: Lidar backscatter ratio assuming no aerosols in the atmosphere. Panel 2: Temperature profile from the lidar backscatter profile for the interval between 14.50 UT on 12 January 2002 and 02.10 UT on 13 January 2002. Horizontal lines are error bars. Panel 3: Buoyancy frequency from the temperature profile in the second panel (solid line) and windshear from winds in Figure 5, "alt. 2" (dotted line). Panel 4: Maximum radar echo power detected between 0 UT on 12 January 2002 and 24 UT on 13 January 2002 (arbitrary units). Dashed line indicates the noise level.

Figure 5. UKMO/ESRAD/SkiYmet winds representing 12 UT on 12 and 13 January 2002, respectively ; 'UKMO' winds are from the assimilated meteorological analysis performed by the UK Meteorological Office and cover altitudes 0 - ca. 55 km : data are for 67°N, at 10°E (o), and 20°E (x). 'ESRAD' winds are from the ESRAD MST radar averaged between 11 and 13 UT, indicated by diamonds, covering 2-11 km altitude. 'SkiYmet' winds are from the meteor radar at the same site as ESRAD, averaged between 10:30 and 13:30 UT, indicated by diamonds, covering altitudes 77-97 km altitude. Zonal winds are labelled 'u' , meridional winds 'v'. Between 55 km and 76 km total windspeed is interpolated in two alternative ways (labelled 'alt. 1' and 'alt. 2' - see text for details)

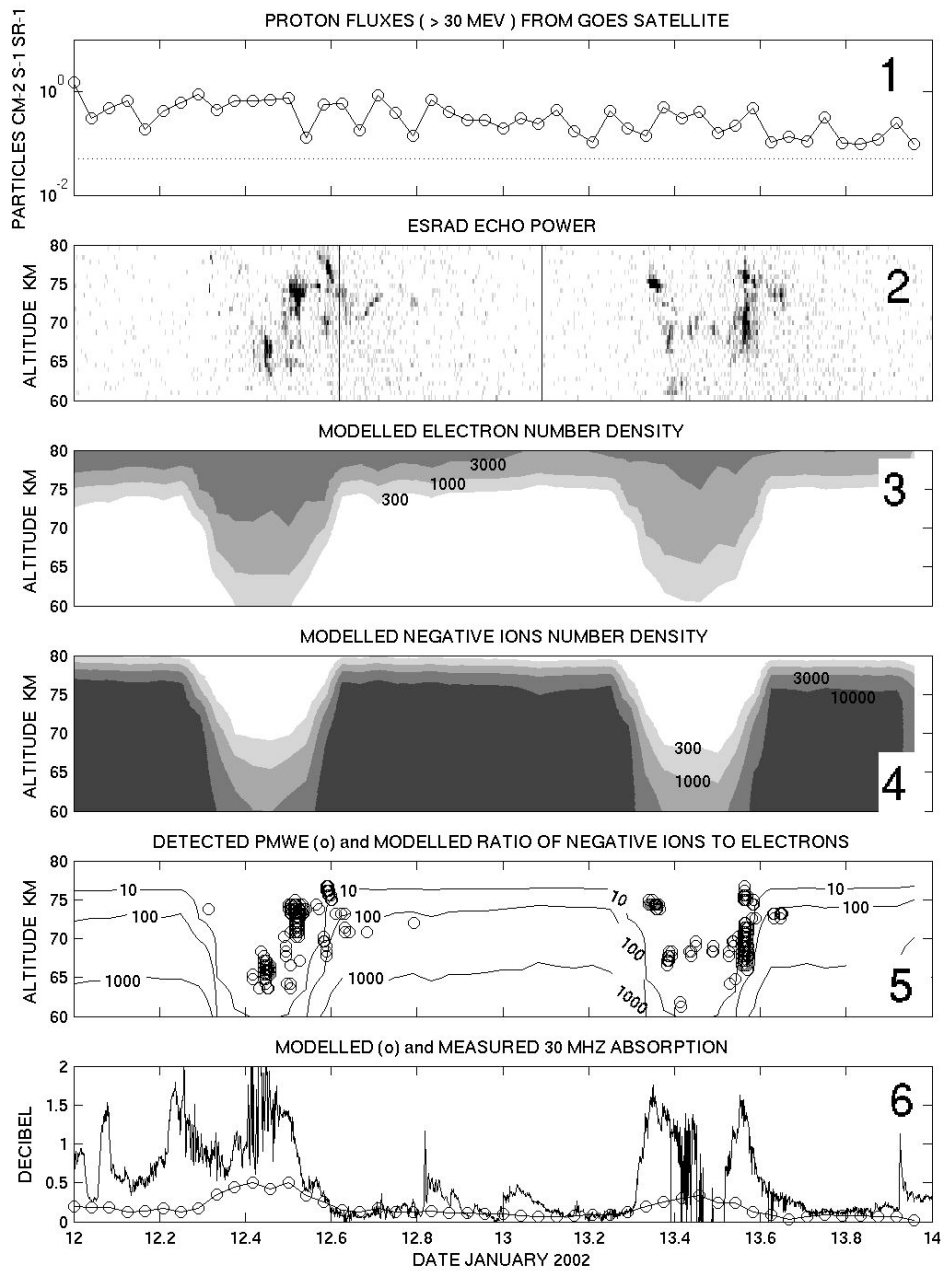


Figure 1 – ESRAD data and model results for 12/13 January 2002. Panel 1: Proton fluxes measured at geostationary orbit (normal undisturbed level is shown by the horizontal dotted line). Panel 2: Signal and noise power detected by the radar, the background (noise) level is 15 dB (white) and the strongest signals exceed 25 dB (black). Vertical lines on the second panel indicate the start and end of the lidar data-

integration period. Panel 3: Electron densities calculated from the proton flux measured by GOES (units cm^{-3}). Panel 4: Calculated negative ion densities (units cm^{-3}). Panel 5: Contours of the ratio of negative ion density to electron density (λ) overlaid with circles indicating times and heights when and where PMWE were detected. Panel 6: Cosmic-noise absorption calculated from the electron densities in the third panel (circles) and absorption measured by the riometer at Abisko, 100 km west of ESRAD.

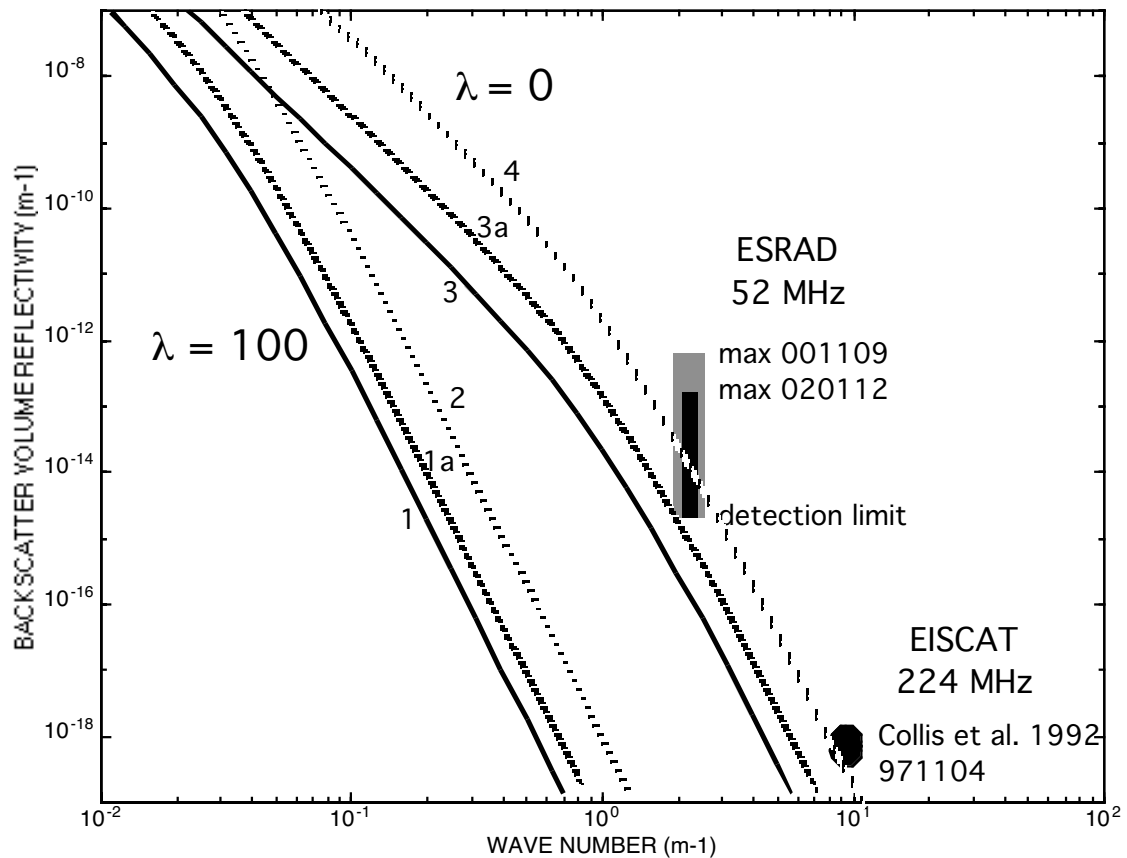


Figure 2. Radar volume reflectivities estimated from radar observations (ESRAD as bars, EISCAT as dots, dates in form YYMMDD) and from turbulence theory (lines). Dates of radar observations are indicated. Calculations from turbulence theory are described in the Appendix. Curve 1 corresponds to electron density $N_e = 3 \times 10^8 \text{ m}^{-3}$, electron-density gradient $dN_e/dz = 9 \times 10^4 \text{ m}^{-4}$, square of Brunt-Väisälä frequency $\Omega_B^2 = 4 \times 10^{-4} \text{ s}^{-2}$; Curve 1a as curve 1 but $\Omega_B^2 = 1 \times 10^{-4} \text{ s}^{-2}$; Curve 2 is for $N_e = 3 \times 10^9 \text{ m}^{-3}$, $dN_e/dz = 9 \times 10^5 \text{ m}^{-4}$, $\Omega_B^2 = 4 \times 10^{-4} \text{ s}^{-2}$; Curve 3 corresponds to $N_e = 3 \times 10^9 \text{ m}^{-3}$, $dN_e/dz = 9 \times 10^4 \text{ m}^{-4}$, $\Omega_B^2 = 4 \times 10^{-4} \text{ s}^{-2}$; Curve 3a as curve 3 but $\Omega_B^2 = 1 \times 10^{-4} \text{ s}^{-2}$; Curve 4 is for $N_e = 3 \times 10^{10} \text{ m}^{-3}$, $dN_e/dz = 9 \times 10^5 \text{ m}^{-4}$, $\Omega_B^2 = 4 \times 10^{-4} \text{ s}^{-2}$. Curves 1, 1a and 2 for dawn/dusk conditions when there are 100 times as many negative ions as free

electrons ($\lambda=100$). Curves 3, 3a and 4 for midday conditions with no negative ions ($\lambda=0$). All curves for energy dissipation rate $\epsilon = 100$ mW/kg, and for height 70 km.

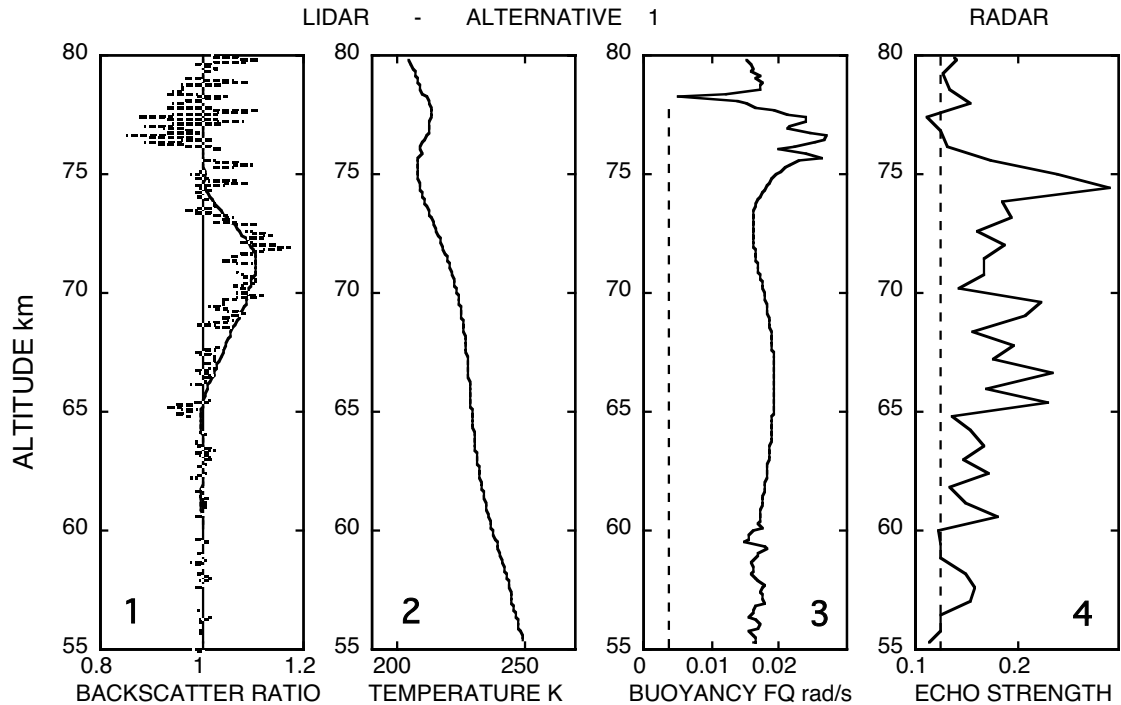


Figure 3 . Panel 1: Lidar backscatter ratio for the interval between 14.50 UT on 12 January 2002 and 02.10 UT on 13 January 2002, assuming a smooth neutral density profile (see text for details). Height resolution is 150 m. Panel 2: Temperature profile corresponding to the smooth neutral density profile. Panel 3: Buoyancy frequency from the temperature profile in the second panel (solid line) and windshear from winds in Figure 5 "alt. 1" (dotted line). Panel 4: Maximum radar echo power detected between 0 UT on 12 January 2002 and 24 UT on 13 January 2002 (arbitrary units). Height resolution is 600 m. Dashed line indicates the noise level.

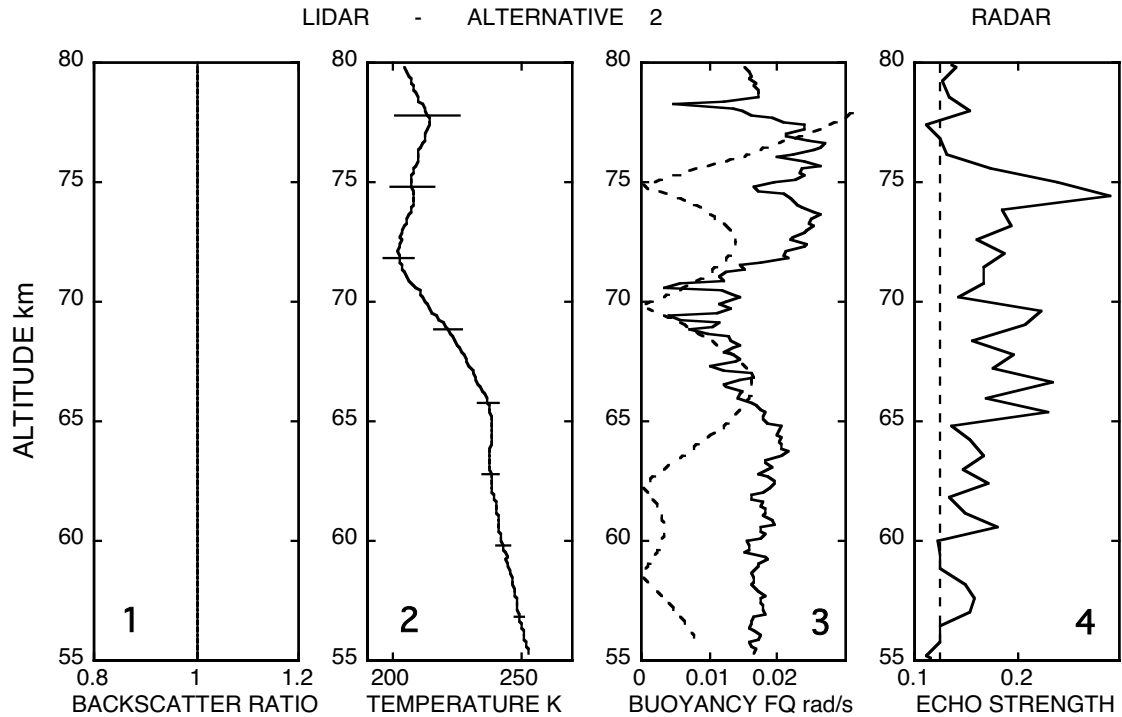


Figure 4. Panel 1: Lidar backscatter ratio assuming no aerosols in the atmosphere. Panel 2: Temperature profile from the lidar backscatter profile for the interval between 14.50 UT on 12 January 2002 and 02.10 UT on 13 January 2002. Horizontal lines are error bars. Panel 3: Buoyancy frequency from the temperature profile in the second panel (solid line) and windshear from winds in Figure 5, "alt. 2" (dotted line). Panel 4: Maximum radar echo power detected between 0 UT on 12 January 2002 and 24 UT on 13 January 2002 (arbitrary units). Dashed line indicates the noise level.

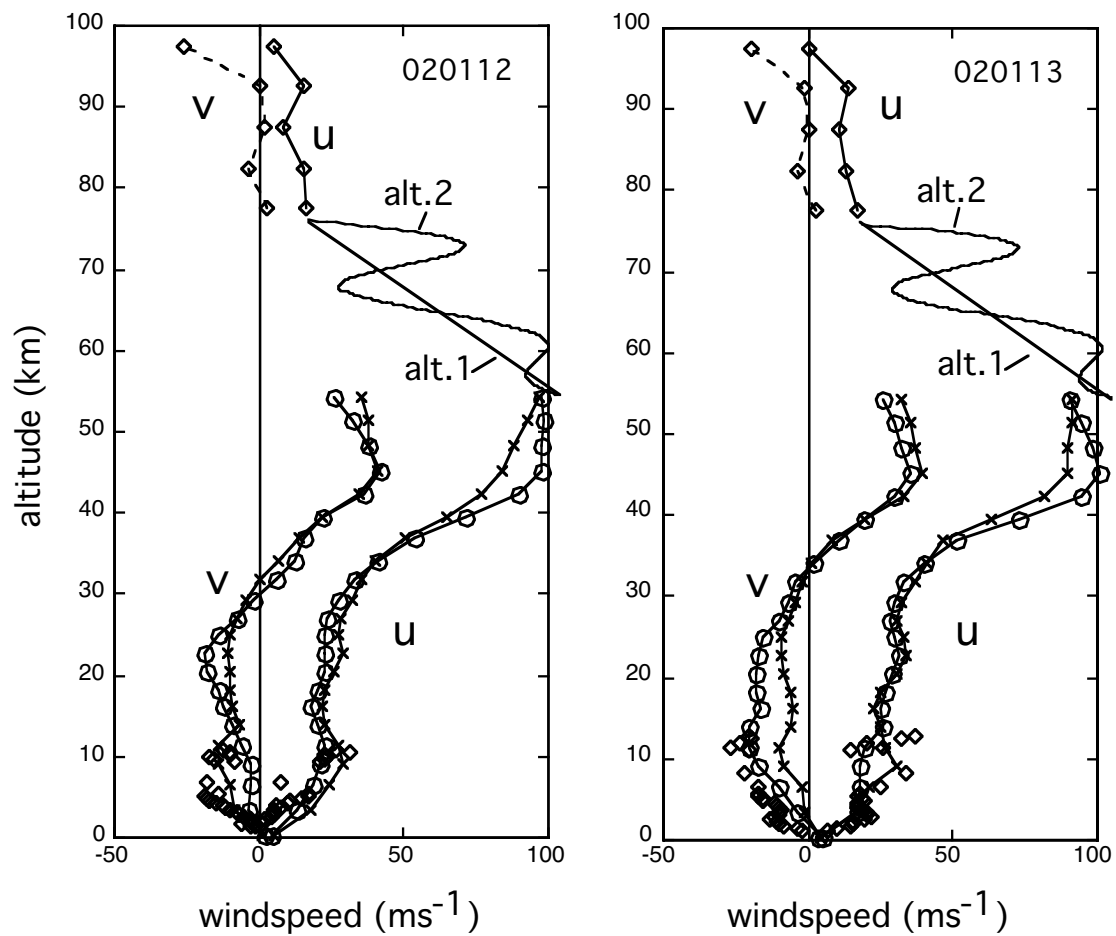


Figure 5. UKMO/ESRAD/SkiYmet winds representing 12 UT on 12 and 13 January 2002, respectively ; 'UKMO' winds are from the assimilated meteorological analysis performed by the UK Meteorological Office and cover altitudes 0 - ca. 55 km : data are for 67°N, at 10°E (o), and 20°E (x). 'ESRAD' winds are from the ESRAD MST radar averaged between 11 and 13 UT, indicated by diamonds, covering 2-11 km altitude. 'SkiYmet' winds are from the meteor radar at the same site as ESRAD, averaged between 10:30 and 13:30 UT, indicated by diamonds, covering altitudes 77-97 km altitude. Zonal winds are labelled 'u' , meridional winds 'v'. Between 55 km and 76 km total windspeed is interpolated in two alternative ways (labelled 'alt. 1' and 'alt. 2' - see text for details)